

1  
2 **Concentrated slip and low rupture velocity for the May 20, 2012, Mw 5.8, Po**  
3 **Plain (Northern Italy) earthquake revealed from the analysis of source time**  
4 **functions**  
5

6 **Authors:**

7 Vincenzo Convertito<sup>1</sup>, Nicola Alessandro Pino<sup>1</sup>, and Davide Piccinini<sup>2</sup>

8  
9 <sup>1</sup>Istituto Nazionale di Geofisica e Vulcanologia, Osservatorio Vesuviano,  
10 Via Diocleziano 328, Napoli, Italy

11  
12 <sup>2</sup>Istituto Nazionale di Geofisica e Vulcanologia, sezione di Pisa,  
13 Via Cesare Battisti 53, Pisa, Italy

14  
15 Corresponding author: Vincenzo Convertito

16 Istituto Nazionale di Geofisica e Vulcanologia, sezione di Napoli Osservatorio Vesuviano, Via  
17 Diocleziano 328, Napoli, Italy

18 Tel.: +390816108343.

19 *E-mail address:* vincenzo.convertito@ingv.it  
20

21 **Keypoints**

- 22 • We use a forward modelling and a Bayesian inverse method to image slip distribution of the  
23 May 20, 2012, Mw 5.8, Northern Italy, earthquake
- 24 • We found a bilateral rupture with concentrated slip
- 25 • We found slow rupture velocity  
26

27 **Abstract**

28 We analyse the rupture properties of the May 20, 2012, Mw 5.8, Po Plain (Northern Italy) earthquake  
29 by using two different modelling procedures based on the source time functions: a forward modelling  
30 and a global inversion Bayesian method. While the forward modelling allows to retrieve general  
31 information on the source characteristics, the global inversion allows to explore a substantially larger  
32 number of possible solutions, with more parameters, providing a quantitative estimate of the misfit.  
33 We inverted for the spatial slip distribution and for the rupture velocity on a planar fault model. The  
34 unknown slip is given at the nodes of the subfaults (control points) and then given at the elementary  
35 subfaults through a bilinear interpolation. The number of control points is progressively increased to  
36 move from a high- to low-wavelength description of final slip on the fault plane. The optimal model  
37 parameter set is chosen according to the Akaike Information Criterion. The uncertainty on the slip  
38 distribution and rupture velocity has been estimated by a statistical analysis of the model ensemble  
39 and, in particular, through the weighted mean model and the standard deviation.  
40 We find that the most earthquake slip occurred in the regions located northeast and southwest of the  
41 hypocenter, consistent with the forward modelling. Moreover, we find a low rupture propagation  
42 velocity (0.4 compressional Mach number) similarly to what has been observed for the close 29 May,  
43 Mw 5.6, and radiation efficiency suggesting that half of the strain energy was used to create new  
44 fracture.

45  
46 **Keywords**

47 Earthquake source kinematics, slip image, source directivity

48

49

50

51

52

## 53 **1 Introduction**

54 The May 2012 seismic sequence occurred in the Po Plain (Northern Italy) and started on May 19,  
55 2012, at 23:13:27 GMT with a  $M_L$  4.1 ( $M_w$  4.0) earthquake. On May 20 a  $M_L$  5.9 ( $M_w$  5.8) event  
56 was recorded, followed by a second  $M_L$  5.8 ( $M_w$  5.6) main shock on 29 May  
57 (<http://cnt.rm.ingv.it/tdmt>, Scognamiglio et al., 2006) and thousands of aftershocks, six of them with  
58 magnitude larger than 5.0 (Govoni et al., 2014) (Figure 1). The sequence took place on a south dipping  
59 blind thrust fault system (Ferrara arc) in the Emilia-Romagna region, covered by the quaternary  
60 sediment of the Po Plain. The largest events in the sequence are indeed characterized by reverse  
61 faulting style (e.g., Malagnini et al., 2012; Ventura and Di Giovambattista, 2013). Based on the Italian  
62 seismic classification the areas interested by the seismic sequence are classified as a low-to-moderate  
63 hazard (Stucchi et al., 2011). Indeed, expected PGA values with 10% probability of exceedance in  
64 475 years range between 0.05 g to 0.25 g (being g the acceleration of gravity). However, the sequence  
65 caused 27 fatalities and widespread severe damage to dwellings forcing the closure of several  
66 factories (Lai et al., 2012). If on one hand part of the damage can be ascribed to site effects  
67 amplification (Castro et al., 2013) and to the performance of the industrial or civil structures (e.g.,  
68 Liberatore et al., 2013; Manfredi et al., 2013; Masi et al., 2013), on the other hand it is important to  
69 understand the characteristics of the seismic source in order to assess its contribution to the general  
70 picture.

71 In spite of its impact, only a few analyses have been published on the source characteristics of the  
72 May 20 earthquake. The preliminary analyses of GPS (Serpelloni et al., 2012) and InSAR data  
73 (Bignami et al., 2012) only derived fault geometry by assuming uniform slip distribution.  
74 Successively, the analysis of the geodetic data (GPS and InSAR) by Pezzo et al. (2013) identified  
75 two main fault planes one oriented  $N114^\circ$  with a maximum slip of about 120 cm at 5 km depth and  
76 one oriented  $N95^\circ$  with slip of about 30 cm between 3 and 7 km. The same study indicates that the  
77 following 29 May,  $M_w$  5.6, event interested this latter plane. However, evidences for complex slip  
78 distribution was brought by Piccinini et al. (2012) who concluded that the rupture clearly features at

79 least two distinct pulses separated by time intervals of about 1.5-2 s, with significant amount of energy  
80 radiated WSW. This complexity was imaged by Ganas et al. (2012), who inferred the distribution of  
81 slip, the rupture velocity, and the rise time of the event, using empirical Green's functions (EGFs) and  
82 a least-squares inversion scheme of source time functions (STFs) computed from regional broadband  
83 seismological data. Conversely, Cesca et al. (2013), studying the directivity effect in the frequency  
84 domain 0.01-0.1 Hz, found that the rupture propagated unilaterally about 15 km towards SE. A similar  
85 rupture propagation direction was found by Convertito et al. (2013) as dominant direction, from the  
86 analysis of the peak-ground accelerations. The variability of the results obtained in the above  
87 mentioned analyses suggests that further investigations are required to better characterize the rupture  
88 history and the slip distribution. The aim of the present study is to analyse the rupture properties of  
89 the largest and most damaging event in the sequence, occurred on May 20. In particular, we analysed  
90 rupture kinematics and image the slip distribution from the analysis of the STFs – obtained by an  
91 empirical Green's functions approach – by using two different modelling procedures based on the  
92 source time functions: a forward modelling and a global inversion Bayesian method. The main  
93 advantage of using the STFs obtained by applying the EGFs technique is that uncertainties in  
94 structural as well as site effect model may be neglected. Indeed, as evidenced by Graves and Wald  
95 (2001), an inaccurate velocity structure could strongly bias the inverted slip distribution even when  
96 the rupture velocity, rise time, and rake angle are fixed. Moreover, the forward modelling allows to  
97 retrieve general information on the source characteristics, while the global inversion method  
98 implemented here allows to solve the nonlinear problem of inverting seismic data for the spatial slip  
99 distribution and rupture velocity on a fault.

100

## 101 **2 Method**

102 The source time function represents the temporal evolution of the seismic moment release during  
103 the propagation of the fracture and contains details about the history of the dislocation. Here we first  
104 apply a deconvolution technique to derive the relative source time functions for the 20 May,  $M_L$  5.9,

105 event and then derive information on the source kinematics by using forward and inverse modelling.  
106 The first approach allows to investigate the features of the STFs and to get a first rough picture of the  
107 rupture propagation (e.g., Convertito et al., 2016), while the inverse modelling leads to a more  
108 complete image of the slip pattern. Both approaches are based on the retrieval of the apparent moment  
109 rates radiated at different azimuths, by applying an empirical Green's function approach (see, for  
110 instance, Mori (2003) and reference therein). This technique consists of the deconvolution, at each  
111 station, of the seismograms relative to a suitable small event from the waveforms of the mainshock.  
112 If the hypocentral location and the source geometry of the two earthquakes are similar enough, the  
113 recording of the small event at a given station can be considered as EGF for that focal mechanism,  
114 i.e., representative of the structure response to an impulsive source characterized by the same fault  
115 geometry, for that specific source-receiver path. The results of the deconvolution represent the  
116 relative source time functions as seen at the relevant azimuth. The higher the corner frequency of the  
117 EGF and closer the small event to the mainshock, the higher the frequency resolution of the resulting  
118 RSTF.

119 In principle, if the mainshock and the EGF have the same location and the same focal mechanism,  
120 their waveforms – filtered below the corner frequency of the large one, i.e., where both events can be  
121 considered as point source – have to be similar at each station. Thus, in order to search for the best  
122 EGF, we first chose a couple of test stations and estimated the corner frequency  $f_c$  of the mainshock  
123 at those sites, by using the method described by Snoke (1987). Then we performed a matched-filtered  
124 analysis, by sliding the waveforms of the mainshock along the continuous seismograms recorded at  
125 the same station throughout the period May 19-June 8, with both signals previously low-pass-filtered  
126 below  $f_c$ . At each time step, we calculated the cross-correlation function, assuming that its maximum  
127 occurs at the time of the best EGF for the analysed event. The results from this procedure have then  
128 been checked by visual inspection of the retrieved seismograms. The preferred EGF is the foreshock  
129 occurred on May 19, 2012, at 23:13:27 GMT with a  $M_L$  4.1 ( $M_w$  4.0) earthquake.

130

## 131 **2.1 Forward modelling**

132 In the forward modelling we considered a simple pulse line source and tested different values for  
133 the kinematic source parameters, by comparing the predicted STFs with the observed ones. The  
134 approach is basically qualitative and aimed at retrieving basic information on the source  
135 characteristics that could also provide hints for interpreting the STFs, thus understanding what are  
136 their most stable and reliable features. This is particularly helpful when dealing with moderate  
137 magnitude events, whose source time functions are often affected by not negligible noise. Indeed, it  
138 has been successfully applied to the 29 December 2013, Matese, southern Italy,  $M_w$  5.0, earthquake  
139 (Convertito et al., 2016).

140 In our approach, we started with a unilateral rupture and attempted at determining the parameters  
141  $t$ ,  $\vartheta_d$ , and  $v_r$  providing a reasonably reproduction of the main features of the observed STFs. The result  
142 should give the main direction of propagation of the rupture and provide a first estimate of the source  
143 duration. Successively we explored the chance of bilateral rupture by adding a second line source  
144 propagating in a different direction and tested different shapes for moment rate by checking simple  
145 functions. When the main parameters are fixed, finally we try to infer possible secondary features in  
146 the shape of the moment rate.

147

## 148 **2.2 Bayesian inversion modelling**

149 Here the direct problem is solved by computing slip at a set of control points (e.g., Emolo and  
150 Zollo, 2005) regularly distributed on the fault plane and then interpolating on a finer grid. To this aim  
151 we used a bilinear interpolation and filtered the slip map by using a Gaussian bi-dimensional filter  
152 (e.g., Király-Proag et al., 2019). The number of control points defines the size of the subfaults and is  
153 selected on the basis of the magnitude of the EGF. Indeed, the minimum size cannot be smaller than  
154 the estimated size of the EGF. Each subfault is characterized by a single fault mechanism and  
155 described by three parameters: the final slip value, the rise time  $\tau$  – defining the source time function  
156 – and the onset time. The size of the finer grid is selected according to the coherent rupture condition

157 of six source points per wavelength (Archuleta and Hartzell, 1981). The method implemented in this  
 158 study prescribes that the number of control points is progressively increased to move from a high- to  
 159 low-wavelength description of final slip and rupture velocity on the fault plane (e.g., Emolo and  
 160 Zollo, 2005). The optimal model parameter is finally chosen according to the minimum of the  
 161 corrected Akaike Information Criterion parameter (Akaike, 1974). Nucleation point was located at  
 162 the fault centre and the rupture propagates at a constant rupture velocity. At each source depth we  
 163 evaluated the  $v_p$  value (i.e., the propagation velocity of the selected seismic phase) using a specific  
 164 crustal model for the area of interest and then computed the Mach number  $\alpha=v_r/v_p$ , being  $v_r$  the  
 165 rupture velocity. Each sub-fault was allowed to slip only once with a triangular slip-rate function  
 166 whose activation time from the origin time depend on the distance from the nucleation point, while  
 167 the apparent activation time also depend on the source position with respect to the specific receiver  
 168 according to the directivity function  $C_d$ . For a fault plane the  $C_d$  function (Ben-Menahem, 1961) is:

169

$$170 \quad C_d = \frac{1}{(1 - \alpha \cos \vartheta_{ri})} \quad (1)$$

171

172 where  $\alpha$  is the Mach-number and  $\cos \vartheta_{ri}$  is given by

173

$$174 \quad \cos \vartheta_{ri} = \cos(\varphi_r - \varphi_i) \sin \zeta_r \sin \zeta_i + \cos \zeta_r \cos \zeta_i \quad (2)$$

175

176 where  $\vartheta_{ri}$  is the angle between the body wave radiated to station  $i$  (at azimuth  $\varphi_i$  and vertical takeoff  
 177 angle  $\zeta_i$ ) and the rupture direction at azimuth  $\varphi_r$  and rupture angle  $\zeta_r$  from vertically down. For each  
 178 station the vertical takeoff angle  $\zeta_i$  was computed by using the adopted crustal model proposed for  
 179 the area by Govoni et al. (2014). Although the EGF approach should allow to theoretically eliminate  
 180 the effect of the propagation medium from the signal of the mainshock the use of the directivity  
 181 function makes it necessary to introduce a velocity model in order to compute the take-off angle.

182 As for the inverse problem, we implemented the Metropolis-Hastings sampler approach to  
 183 investigate the model space parameter. Since for a given model  $\mathbf{m}$  the next candidate point is  
 184 generated as  $\mathbf{m}_t = \mathbf{m}_{t-1} + \mathbf{z}$  where  $\mathbf{z}$  is an increment random variable from a proposal distribution  $f$ , the  
 185 approach corresponds to the random-walk Metropolis. The components of  $\mathbf{m}$  are the rupture velocity  
 186  $v_r$ , the rise-time  $\tau$ , and the slip distribution at a given number of points (control points). The best  
 187 model parameter corresponds to the model that maximize the posterior distribution of the model space  
 188 parameters, which is given by

$$190 \quad f(\mathbf{m}|\mathbf{d}) = \frac{f(\mathbf{d}|\mathbf{m})\rho(\mathbf{m})}{\int_{\Omega} f(\mathbf{d}|\mathbf{m})\rho(\mathbf{m}) d\mathbf{m}} \quad (3)$$

191  
 192 where  $\mathbf{d}$  is the data vector and  $\mathbf{m}$  is the model vector selected in the model space  $\Omega$ ,  $\rho(\mathbf{m})$  is the priori  
 193 distribution and  $f(\mathbf{d}|\mathbf{m})$  is the likelihood function given by

$$194 \quad f(\mathbf{d}|\mathbf{m}) = c e^{-Misfit} \quad (4)$$

195  
 196  
 197 and

$$198 \quad Misfit = \frac{\sum_{i=1}^{Nstaz} \sum_{j=1}^{Nt} (S_{ij}^{cal} - S_{ij}^{obs})^2}{\sum_{i=1}^{Nstaz} \sum_{j=1}^{Nt} S_{ij}^{obs^2}} \quad (5)$$

199  
 200  
 201 In equation (4)  $c$  is a normalization constant while in equation (5)  $Nstaz$  is the number of available  
 202 stations and  $Nt$  is number of points of the source time functions  $S_i$ . As for the models' selection, after  
 203 a given burn-in period, that is, a given number of iterations (e.g. the first 1,000 or so) (Gelman et al.,  
 204 2004), a candidate model  $\mathbf{m}_i$  is accepted if  $f(\mathbf{d}|\mathbf{m}_i) > f(\mathbf{d}|\mathbf{m}_{i-1})$ , otherwise it is accepted if the acceptance  
 205 ratio  $f(\mathbf{d}|\mathbf{m}_i)/f(\mathbf{d}|\mathbf{m}_{i-1})$  is larger than  $\eta$ , where  $\eta$  is a number ranging between 0 and 1, randomly



206 extracted from an uniform distribution. The advantage of using the ratio of the  $f(\mathbf{d}|\mathbf{m}_i)$  functions is  
 207 that it allows to avoid the computation of the normalization constant in equation (4) and to neglect  
 208 the prior distribution thus reducing the problem of finding the maximum of the posterior distribution  
 209  $f(\mathbf{m}|\mathbf{d})$  to minimizing the misfit function reported in equation (5). At each iteration, the candidate  
 210 models are obtained by using as proposal distribution a uniform distribution for both the rupture  
 211 velocity and the rise-time, and the slip value at each control point. Similar to what has been done by  
 212 Liu et al. (2006), we run the procedure 30 times starting from a different seed each time. From the  
 213 analysis of the misfit of each model we identified the model with the lowest misfit and used the first  
 214 15 models to calculate the ensemble properties (e.g., Piatanesi et al., 2007). In particular, we  
 215 considered the weighted average of slip maps using the misfit as weight, and the map of standard  
 216 deviations. While the first allows the identification of the coherent features of the models, the standard  
 217 deviation map allows us to estimate the uncertainty on the slip values in the different portions of the  
 218 fault.

219 Next, starting from the slip map we computed a static stress drop map (Mai and Beroza, 2002;  
 220 Guatteri et al., 2004). To this aim we used the relation between slip and stress proposed by Andrews  
 221 (1980):

$$\Delta\sigma(\mathbf{k}) = -K(\mathbf{k}) \cdot D(\mathbf{k}) \quad (6)$$

224 where  $\Delta\sigma(\mathbf{k})$  denotes the 2D transform in the wavenumber domain of the stress drop function and  
 225  $D(\mathbf{k})$  the transform of the slip function.  $K(\mathbf{k})$  represents the static stiffness function that for crustal  
 226 rocks can be approximated as:

$$K(\mathbf{k}) = -\frac{1}{2}\mu k \quad (7)$$

230

231 where  $\mu$  is the shear modulus (assumed as  $3.3\text{e}+10$  Pa) and  $k = \sqrt{k_x^2 + k_y^2}$  (Andrews, 1980). By  
 232 using the stress drop distribution and the approach proposed by Guatteri et al. (2004), we computed  
 233 the distribution of fracture energy  $G_c$ , that is, the amount of energy required to make the crack surface  
 234 advance per unit surface (e.g., Rivera and Kanamori, 2005; Lancieri et al., 2012). In particular,  
 235 Guatteri et al. (2004) provide an empirical relationship to compute  $G_c$ , once the stress drop map has  
 236 been computed, that for event with magnitude lower than 6.5, is given by:

237

$$238 \quad E(G_c|\boldsymbol{\beta}, \Delta\sigma, L_h) = 0.18 + 0.0015\Delta\sigma L_h^{1/2} \quad (8)$$

239

240 where  $E(G_c|\boldsymbol{\beta}, \Delta\sigma, L_h)$  indicates the expected value of  $G_c$ ,  $\boldsymbol{\beta}$  is the vector containing the intercept and  
 241 slope of the linear relation,  $\Delta\sigma$  is the static stress drop, and  $L_h$  is the crack length computed as the  
 242 distance of each point on the fault from the nucleation point as defined by Guatteri et al. (2004).

243

### 244 **3 Results**

245 We deconvolved the waveforms of the relevant EGF from those of the mainshock by spectral ratio  
 246 with watering level correction, restricting the computation to the  $P$ -wave train. We selected  
 247 broadband stations (all sampled at 100 Hz) within 250 km from the epicenter and used the vertical  
 248 components. For each station, we performed several deconvolutions by slightly changing the  $P$ -wave  
 249 train duration and verified that it did not affect the final STFs, giving stable results. Thus, we finally  
 250 derived apparent moment rates at 12 stations and low-pass filtered the results at 1 Hz (Figure 2), well  
 251 below the corner frequency of the EGF (3 Hz). We remark that at all the selected stations the signal-  
 252 to-noise ratio (corresponding to the ratio between the mean amplitude of 10 s signal before and 10 s  
 253 after the  $P$ -wave of the EGF) is higher than 20 (e.g., Figure 2).

254 The available sites are fairly well distributed with respect to the epicenter, with azimuthal gaps of  
 255  $93^\circ$  and  $80^\circ$  on the west and on the east side, respectively (inset in Figure 1). We note that, although

256 the selected EGF is the best among the available aftershocks (according to the match filtering  
257 analysis), the resulting STFs still may be affected by the effect of small differences on the hypocentral  
258 location and focal mechanism between the mainshock and the selected aftershock.

259

### 260 **3.1 Forward modelling**

261 Overall, the relative STFs (RSTFs) display quite distinct waveforms at the various azimuths, with  
262 the largest amplitudes and frequencies at stations located South-West of the epicentre – between  
263 N200° and N230° – where a sharp pulse is well visible, while clearly smoother functions result to the  
264 N-NE. The breakage of symmetry indicates that some directivity effect is present and the features  
265 remarked above point to possible preferential rupture propagation toward the SW quadrant. However,  
266 both the duration and the maximum amplitude of the RSTFs do not change dramatically with azimuth.  
267 Incidentally, we notice that the total apparent duration is always larger than 7 s, with the minimum at  
268 PARC (source-to-station azimuth N149°), indicating that the actual total rupture cannot last less than  
269 that. If simple unilateral breakage occurred, RSTFs with significantly longer duration and lower  
270 amplitude should have resulted on one side. Instead, the lowest maximum amplitudes are indeed  
271 displayed at the station located N-NW of the source, but these are not associated with the longest  
272 durations. These observations suggest a complex pattern of rupture propagation.

273 In order to obtain indications on the source kinematics, we performed a direct modelling of the  
274 retrieved moment rates. We first focused on matching the most energetic peak of the observed STFs.  
275 Thus, we started by assuming a unilateral rupture source with simple gaussian moment rate and, by  
276 testing different rupture velocity values, we changed source duration and amplitude at the various  
277 azimuths according to the directivity equation  $t_a = L(1/v_r - \cos \vartheta / v_p)$ , with  $t_a$ ,  $L$ , and  $v_r$   
278 respectively indicating the apparent duration, the rupture length, and the rupture velocity; while  $\vartheta$  is  
279 the angle between the source-to-station direction and the rupture direction and  $v_p$  the  $P$  wave velocity  
280 in the source area. As for the rupture velocity, we tested a few values in the range 2.0 - 2.4 km/s that,  
281 however, given the complexity of the observed STFs and the simplistic assumed linear model, did

282 not allow to discriminate a reliable best value. Thus we decided to use the average 2.2 km/s value.  
283 Based on the above observations, we used a source propagating toward the SW quadrant ( $\vartheta_d=225^\circ$ ),  
284 with rupture duration  $t_d=7$  s, and rupture velocity  $v_r=2.2$  km/s – resulting in  $L=15.4$  km – and  $v_p=5.5$   
285 km/s (Figure 3). The distinct durations and amplitudes displayed by the resulting functions indicate  
286 that, for the assumed source parameters, the apparent durations and amplitudes can be considered  
287 appropriate to give indications on possible preferential rupture directions. Moreover, the variation of  
288 the synthetic moment rate function with azimuth indicates that angle differences around  $30^\circ$  can be  
289 resolved. As for the actual source, the simple unilateral rupture accounts for the shape (frequency) of  
290 the main pulse present in the data. However, the model rupture predicts too low amplitude at opposite  
291 azimuth, where apparently considerable energy was actually propagated. Besides, the actual  
292 waveforms at the SW stations display some later energy that appears to be shorter at stations in the  
293 SE quadrant and rapidly smearing at other azimuths. These evidences imply that the source of May  
294 20 event must have released a significant seismic moment amount SW of the epicenter, but also that  
295 the rupture corresponds to a more complex rupture than a simple unilateral fracture.

296 Thus, we started with the assumption of purely symmetric bilateral fracture, with two equal sub-  
297 events propagating toward opposite directions, and simply added a second source with 7 s duration  
298 as well, but propagating toward  $N45^\circ$ . We used trapezoidal moment rate functions, more similar to  
299 the pulses observed in the data. It should be noticed that, at this level, we were interested at getting  
300 general information on the source directivity and not focused yet on the determination of realistic  
301 rupture lengths. The predicted RSTFs (Figure 3) display similar amplitude at all azimuth, similar to  
302 what observed in the data, supporting the hypothesis of multiple rupture propagating in definitely  
303 distinct – possibly opposite – directions. In addition to this basic consideration, the comparison  
304 addresses a few more points. The main pulse of the  $N225^\circ$  source must be significantly shorter than  
305 what assumed. But, also, moving clockwise from  $N300^\circ$  to  $N60^\circ$  the total duration of the actual  
306 RSTFs increases, indicating that, at those stations, the final part of the moment rate is to be due to  
307 SW propagating source. These two observations imply that the  $N225^\circ$  propagating rupture do lasts

308 about 7 s, like the model pulse; but it also has to be asymmetric, with a major sharp pulse in the first  
309 few seconds. On the other hand, moving clockwise from N300°, the initial ramp in the data becomes  
310 higher and steeper, meaning that this energy must be associated to a rupture propagated  
311 approximately eastward. Although the synthetic RSTFs well reproduce this feature, the N45°  
312 propagation azimuth also predicts a much faster variation than what observed, suggesting that this  
313 second rupture patch should have propagated at a larger angle from N. For what noted above, the two  
314 sub-events must be superimposed in time.

315 Starting from these observations, we made a further test (Figure 3), with the N225° source shaped  
316 as described above, while for the second rupture we used a larger propagation angle. Based on the  
317 focal mechanism of the May 20, 2012 (INGV-TDMT catalogue at <http://cnt.rm.ingv.it/tdmt.html>,  
318 Scognamiglio et al., 2006) and on the depth distribution of the aftershocks (Govoni et al., 2014),  
319 which indicate that the fault plane associated with the earthquake has strike directed to N103° and  
320 dip angle of 46°, as a tentative value we assumed N103° for the second rupture direction. The results  
321 are very satisfactory, with the major features – evidenced above – well reproduced. In particular, the  
322 model sources predict the observed distribution of both relative duration and amplitude, also  
323 producing the very similar moment rates observed northwest of the epicenter, the higher frequency  
324 observed to southern sites, and smoother apparent source time functions at the other stations.

325 Overall, the total durations appear to be correct. This means that, if larger rupture velocities  $v_r$  are  
326 imposed, the length  $L$  should also increase, reaching very large values (larger than 23 km) for a  
327  $M_w=5.8$  earthquake (e.g., Wells and Coppersmith, 1984). Similarly, reducing  $L$ , the rupture velocity  
328 would be too low (lower than 1.55 km/s). For these reasons, we consider that adequate rupture  
329 parameters can be considered within  $\pm 30\%$  of the adopted values. As for the  $P$  wave velocity in the  
330 source area  $v_p$ , it affects the results only to a very small extent: a 10% difference of  $v_p$  would result in  
331 2% maximum variations of both duration and amplitude of the synthetic moment rate functions.

332 By considering the focal mechanism, our solution would correspond to a first sub-event rupturing  
333 obliquely about 15 km down-dip (the hypocentral depth is  $z < 7$  km (Govoni et al., 2014)), followed

334 by a second fracture directed approximately eastward, parallel to the fault strike and approximately  
335 15 km-long as well. In our modelling test, the two sub-events are associated with a similar amount of  
336 seismic moment, 45% and 55% of the total  $M_0 = 7.00359E+17$  Nm, respectively for the N225° and  
337 the N103° rupture directions. In order to get an estimate of the peak slip for the two rupture patches  
338 – which cannot be directly deduced by the observed STFs – we independently considered the two  
339 source time function deduced from the forward modelling and applied the modified Haskell source  
340 model used by Kanamori et al. (1992) to determine the slip distribution of the 1990 Landers  
341 earthquake. In particular, by stretching the moment rate to match the rupture length, it can be divided  
342 by the rupture velocity to give the seismic moment per unit length  $m(l) = \mu wd$ , where  $\mu$  is the rigidity,  
343  $w$  the rupture width, and  $d$  the slip. Therefore, dividing  $m(l)$  by  $\mu w$  theoretical slip distributions along  
344 the rupture patches result. Albeit this scheme represents a crude approximation, it already proved to  
345 be effective in a number of cases, for both recent and historical seismic event (e.g., Pino et al., 1999;  
346 Pino et al., 2008), always giving results consistent with the geodetic and independent seismological  
347 analyses, when available. This model assumes unilateral fault propagation, thus we considered each  
348 sub-event as a separate source and converted the moment rate into slip distribution along the direction  
349 of propagation of that specific fracture. As we assumed very simple moment rate functions, rather  
350 than imaging the slip distribution we were interested in getting hints about the maximum slip location  
351 and amplitude for the two rupture patches. For  $\mu = 3 \times 10^{10}$  N/m<sup>2</sup> and  $w = 3$  km, we got maximum slip of  
352 0.53 m for both sub-events; the first located approximately between 3 km and 6 km from the  
353 hypocenter moving down-dip and southwest, the second eastward of the epicentre, along the fault  
354 plane.

355

### 356 **3.2 Inverse modelling**

357 The STFs measured as reported in the previous sections are resampled at 0.05 s before  
358 implementing the inversion approach. We used a fault plane with length 26 km, width 12 km, and  
359 fault mechanism strike 103°, dip 46° and rake 92° as given by TDMT (INGV-TDMT catalogue at

360 <http://cnt.rm.ingv.it/tdmt.html>, Scognamiglio et al., 2006) corresponding to a reverse fault. The  
361 location of the fault centre used as reference point, is at latitude 44.858 and longitude 11.298, at depth  
362 of 1 km corresponding to the top of the fault, while the nucleation point is located at 0 km along the  
363 strike and 7 km downdip. The dimension of the elementary faults is  $0.06 \times 0.06$  km<sup>2</sup>. The rupture  
364 velocity is explored in the range 1.6-3.6 km/s with steps of 0.1 km/s, while we set the rise-time at 0.4  
365 s. The latter is selected by using the relationship between rise-time and  $M_0$  provided by Somerville et  
366 al. (1999). The a-priori slip distribution to be used in the equation (3) is selected as uniform, while  
367 the slip at each control point is perturbed by extracting random values in the range 0.0 to 0.7 m. The  
368 final slip maps are tapered on the border of the fault to avoid unrealistic stopping phases and the total  
369 radiated seismic moment is checked against the actual one by allowing a discrepancy of 25% allowing  
370 a discrepancy of 25% checks the total radiated seismic moment.

371 We tested different number of control points configurations moving from high- to low-wavelength.  
372 For each control point configuration, we run 10 distinct procedure each exploring 10,000 models.  
373 Next, we compute the average model, which is used as starting model for the subsequent control  
374 points configuration. We use the Akaike Information Criterion (AIC) (Akaike, 1974) to select the  
375 best configuration. In particular, we searched for the minimum of the parameter  
376  $AIC=2N_p+N[\ln(2\pi\hat{L})+1]$ , where  $N$  is number of data (the product of number of STF samples and the  
377 number of STFs),  $N_p$  is the number of parameters for each configuration and  $\hat{L}$  is the corresponding  
378 misfit value. For the investigated configurations we obtained:  $3 \times 2$  ( $\hat{L}=0.01050$ ),  $4 \times 3$  ( $\hat{L}=0.01114$ ),  
379  $5 \times 4$  ( $\hat{L}=0.01108$ ),  $6 \times 5$  ( $\hat{L}=0.01030$ ),  $7 \times 6$  ( $\hat{L}=0.01154$ ),  $8 \times 7$  ( $\hat{L}=0.01079$ ), and  $9 \times 8$  ( $\hat{L}=0.01198$ ). The  
380 test indicates that, excluding the configuration  $3 \times 2$  that corresponds to a very high wavelength  
381 configuration, the model with  $8 \times 7$  points along the strike and along the dip, respectively, provides  
382 the optimal compromise between model simplicity and adherence to data (Akaike, 1974). As reported  
383 in the Method section we run the procedure, consisting of 10,000 iterations, 30 times starting from a  
384 different seed each time. We identified as best model the one with the lowest misfit among the 30  
385 results. Then we used the first 15 models identified according to their misfit value to calculate the

386 ensemble properties (e.g., Piatanesi et al., 2007). In particular, for both the slip distribution and the  
387 rupture velocity, we computed the weighted mean model (where the weight is the inverse of the misfit  
388 value) and the standard deviation.

389 The best slip distribution is shown in Figure 4 indicating that the maximum slip value is 0.6 m and  
390 featuring at least two dominant directions. The first is along the strike of the fault while the second is  
391 toward southeast in agreement with the results of the direct approach obtained in this study.  
392 Remarkably, our slip distribution is in very good agreement with independent results obtained from  
393 the geodetic data obtained by Pezzo et al. (2013). On the other hand, Cesca et al. (2013) found a  
394 unilateral rupture direction, oriented toward SE. This difference is mainly due to the fact that Cesca  
395 et al. (2013) analysed a lower frequency range (0.01 – 0.1 Hz), which, for this earthquake, allowed  
396 them to search only for the best unilateral rupture direction. However, we note that their rupture  
397 direction corresponds to the vector sum of the two dominant rupture directions found in our study.  
398 Above the hypocenter and its surrounding region, the fault has slipped with amplitude 30% lower  
399 than that of two main patches. We note that these minor patches are not present in the geodetic  
400 solutions and thus are likely of limited extent and associated with high frequency radiation.  
401 Consequently, they could not be resolved by the forward modelling.

402 The fit between the observed and synthetic STFs corresponding to the best model are shown in  
403 Figure 5 in the time domain and in Figure 6 in the frequency domain. Given the complexity of the  
404 observed STFs and the large areas not covered by the seismic stations in the suitable distance range  
405 the fit is quite satisfactory since it indicates that all the stations have a correlation coefficient larger  
406 than 0.7. The mean slip map and the map of the associated standard deviation are shown in Figure 7.  
407 We observe that the mean slip map suggests that the principal characteristics of the best model  
408 depicted in Figure 4a are a coherent feature of almost all the results obtained from the 15 selected  
409 lower misfit models. Moreover, the standard deviation map indicates that the largest part of the best  
410 slip map is well resolved. When evaluating the fit quality it should be taken into account that part of  
411 the inconsistencies may be due to the fact that some stations are located close to the nodal planes of



412 both the main event and the EGF, thus small differences can affect the retrieved EGF (see for instance  
413 PARC and ASQU locate at similar azimuth but displaying significantly distinct STF). Moreover,  
414 we have assumed a planar fault and constant rupture velocity, which might be simplistic assumptions  
415 for earthquakes occurring in a geological context as complex as the Po Plain-Northern Apennines  
416 region (e.g., Tondi et al., 2019).

417 The best velocity rupture value is  $1.7\pm 0.2$  km/s. Considering that the slip occurred in Jurassic  
418 limestones and upper Triassic carbonates (Bonini et al., 2014), and assuming the crustal model  
419 proposed by Govoni et al. (2014) – which indicates  $v_p \geq 5.7$  km/s for these layers – the inferred  
420 rupture velocity value provides a relatively low compressional Mach number of 0.3 (corresponding  
421 to a shear wave Mach number of 0.5). A similar slow rupture velocity has been observed also for the  
422 close 29 May, Mw 5.6, event (Causse et al., 2017) and interpreted as the fact that the fault was hard  
423 to break and that the fault strength was high in comparison to the initial stress level.

424 Finally, the map of the static stress drop (see Method section) is shown in Figure 4b along with  
425 the aftershocks recorded in the first month after the mainshock (Govoni et al., 2014) and projected  
426 on the fault plane. The result indicates a maximum stress drop of about 3.6 MPa, which is in  
427 agreement with the value of 2.9 MPa obtained by Castro et al. (2013) from the analysis of the S-wave  
428 spectral amplitude decay and that, as expected, the aftershocks occur around the main patches.

429 In order to strengthen this interpretation, we computed the apparent stress and the radiation  
430 efficiency from the analysis of the S-wave spectra. We first analysed acceleration spectra at all the  
431 26 available stations (Figure 8). However, due to the signal-to-noise ratio we obtained stable spectra  
432 at only 8 stations (Table 1). Following Castro et al. (2013) we corrected the observed spectral  
433 amplitude for the near surface attenuation (Anderson and Hough, 1984) using  $K_0 = 0.03$  and used the  
434  $Q$  frequency dependent function for the anelastic attenuation  $Q(f) = 80f^{1.2}$  proposed by Castro *et al.*  
435 (2013) for the area under study. Next, assuming a  $\omega^{-2}$  spectrum (Brune, 1970) we fit the observed  
436 spectra – through a grid search approach – in order to estimate seismic moment ( $M_0$ ), corner  
437 frequency ( $f_c$ ), static stress ( $\Delta\sigma = 0.44 M_0/r^3$ ) and seismic energy. Static stress drop has been

438 computed using the Brune's (1970) model for the corner frequency versus circular rupture radius  
 439 relationship ( $r = 0.37v_s / f_c$ , being  $v_s$  the S-wave velocity, assumed  $2.44 \text{ kms}^{-1}$  as indicated by Castro  
 440 *et al.*, 2013). Seismic energy is measured from the integral of squared ground motion velocity  
 441 computed in the frequency domain,  $I_c$  (Boatwright and Fletcher, 1984):

442

$$443 \quad E_s = \frac{4\pi\rho c R^2}{F^2} I_c = \frac{4\pi\rho c R^2}{F^2} \frac{1}{\pi} \int_0^{\infty} \omega^2 |U(\omega)|^2 d\omega \quad (9)$$

444

445 where  $R$  is the hypocentral distance,  $\rho$  the density,  $c$  the S-wave velocity and  $F$  the free surface  
 446 coefficient. In eq. (9)  $I_c$  is measured in  $(\text{m/s})^2$  and  $E_s$  is expressed in Joule. As proposed by Zollo *et*  
 447 *al.* (2014) we computed the displacement spectrum  $U(\omega)$  from the best-fitting spectral model  
 448 corrected for the frequency band limitation (e.g., Ide and Beroza, 2001). Seismic energy is then used  
 449 to compute the apparent stress  $\tau_a = \mu E_s / M_0$  (Wyss, 1979) with  $\mu$ , the crustal shear modulus, set to  
 450  $3.3 \cdot 10^{10} \text{ Pa}$ . We obtained  $f_c = 0.16 \text{ Hz}$  (0.11, 0.22),  $\Delta\sigma = 2.9 \text{ MPa}$  (0.9, 8.7),  $\tau_a = 1.2 \text{ MPa}$  (0.4, 3.4),  
 451  $E_s = 6.7\text{E}+13 \text{ J}$  (5.9E+12, 9.8E+14). The uncertainties, which correspond to the 95% confidence  
 452 intervals, have been computed by using the technique proposed by Prieto *et al.* (2007). The inferred  
 453 value of corner frequency and static stress drop are in agreement with the values obtained by Castro  
 454 *et al.* (2013). Using the apparent stress drop and the static stress drop we compute the radiation  
 455 efficiency as  $\eta_{sw} = \tau_a / \Delta\sigma$  providing 0.41.

456 In order to obtain a model independent estimate of  $\eta_{sw}$  we neglected the heat energy and computed  
 457 the ratio between the radiated energy  $E_s$  and the total energy  $E_s + E_G$ , where  $E_G$  is total fracture energy.  
 458 We used the stress drop map and the slip map inferred from the inverse modelling to compute the  
 459 fracture energy density  $G_C$  map (Figure 4c). The result indicates a correlation between slip, stress  
 460 drop and fracture energy with the highest value of  $G_C$  spent for fracturing the three main patches and,  
 461 in particular, the downdip one. Thus, from  $G_C$  we computed  $E_G$  over the fault area, obtaining  $E_G$   
 462  $= 7.6\text{E}+13 \text{ J}$ , which leads to a radiation efficiency of 0.47, confirming the estimate obtained by using

463 the Brune model. This result indicates that more than half of the available energy was spent to  
464 propagate the rupture.

465

#### 466 **4 Conclusion**

467 We have investigated the kinematic of the May 20, 2012, Mw 5.8, Po Plain (Northern Italy)  
468 earthquake from the analysis of the source time functions measured at 12 stations. In particular, we  
469 image the final slip map and the rupture velocity. To this aim we have implemented a twofold  
470 approach. The first is a forward modelling that was applied to investigate the rupture characteristics  
471 of the 29 December 2013, Matese, southern Italy, Mw 5.0, earthquake. The second approach is a  
472 multiscale Bayesian nonlinear inverse approach.

473 The two approaches provide consistent results, helping in defining the most robust features of the  
474 asperity breaking during the May 20, 2012, Mw 5.8, Po Plain (Northern Italy) earthquake. The whole  
475 picture suggests that the rupture was bilateral, characterized by two main slip patches of about 0.6 m,  
476 with a significant downdip component. These findings are in accordance with the results obtained by  
477 Pezzo et al. (2013) from the analysis of geodetic data.

478 The rupture propagation velocity resulted in 1.7 km/s, which is notably low and in line with the  
479 value found by Causse et al. (2017) for the close 29 May, Mw 5.6, event. By estimating apparent  
480 stress and static stress drop from S-wave spectral amplitudes, we derived a radiation efficiency of  
481 0.41, which corresponds to half of the available energy spent to create new fracture, indicating a fault  
482 not too hard to break. Thus, rather than the effect of fault strength we suggest that the low rupture  
483 velocity for the two main shocks in the sequence might be controlled by geometrical complexity.  
484 Indeed, it has been suggested that both events occurred on listric faults – with significant dip change  
485 with depth – embedded in the Ferrara arc, a complex geological and structural framework (e.g., Tondi  
486 et al, 2019; Causse et al., 2017).

487 The analysis of the static stress drop deduced from the slip distribution identifies the area of  
488 maximum slip as an asperity and suggests that the rupture stopped at a final stress level close to the

489 kinematic friction level.

490 As for the role of the seismic source characteristics to the observed damage distribution, we  
491 observe that the detected damage pattern (Tertulliani, et al., 2012) exhibits two main lobes of higher  
492 damage in correspondence of the two dominant rupture directions inferred in our study. We conclude  
493 that the notably low rupture velocity contributed significant energy at low frequencies. This reflected  
494 in recorded peak ground velocities higher than predicted by the ground motion predictive equations  
495 (Barnaba et al., 2014), differently from peak ground acceleration in line with the expected values.  
496 Higher energy at low frequency could also explain the serious damage for industrial plants, which  
497 have natural period greater than that of ordinary buildings (Mucciarelli and Liberatore, 2014).

498

#### 499 **Acknowledgments and Data**

500 The authors thank the Associated Editor, Dr Françoise Courboulex and an anonymous reviewer  
501 for their comments and suggestions that helped to improve the manuscript. Focal mechanisms are  
502 available at <http://cnt.rm.ingv.it/>. Waveforms have been downloaded from [http://www.orfeus-](http://www.orfeus-eu.org/data/eida/)  
503 [eu.org/data/eida/](http://www.orfeus-eu.org/data/eida/). Figures were generated with Generic Mapping Tools (GMT; Wessel and Smith,  
504 1991). The present study has been partially supported by Pianeta Dinamico-Working Earth INGV  
505 Project.

506

#### 507 **References**

- 508 Andrews, D. J. (1980). A stochastic fault model, 1. Static case. *J. Geophys. Res.*, 85(B7), 3867–  
509 3877. <https://doi.org/10.1029/JB085iB07p03867>
- 510 Archuleta, R. J., & Hartzell, S.H. (1981). Effects of fault finiteness on near-source ground motion.  
511 *Bull. Seism. Soc. Am.*, 71, 939–957.
- 512 Barnaba, C., Laurenzano, G., Moratto, L., Sukan, M., Vuan, A., Priolo, E., Romanelli, M., & Di  
513 Bartolomeo, P. (2014). Strong-motion observations from the OGS temporary seismic

514 network during the 2012 Emilia sequence in northern Italy. *Bull. Earthq. Eng.*, 12, 2165–  
515 2178. <https://doi.org/10.1007/s10518-014-9610-4>

516 Beeler, N. M., Wong, T. F., & Hickman, S. H. (2003). On the expected relationships among  
517 apparent stress, static stress drop, effective shear fracture energy, and efficiency. *Bull.*  
518 *Seismol. Soc. Am.*, 93, 1381–1389. <https://doi.org/10.1785/0120020162>

519 Ben-Menahem, A. (1961). Radiation of seismic surface waves from finite moving sources. *Bull.*  
520 *seism. Soc. Am.*, 51(3), 401–435.

521 Bignami, C., et al. (2012). Coseismic deformation pattern of the Emilia 2012 seismic sequence  
522 imaged by Radarsat-1 interferometry, *Ann. Geophys.*, 55, 4. <https://doi.org/10.4401/ag-6157>

523 Bonini, L., Toscani, G., & Seno, S. (2014). Three-dimensional segmentation and different rupture  
524 behavior during the 2012 Emilia seismic sequence (Northern Italy), *Tectonophysics*, 630,  
525 33–42, <http://dx.doi.org/10.1016/j.tecto.2014.05.006>

526 Brune, J. N. (1970), Tectonic stress and the spectra of seismic shear waves from earthquakes, *J.*  
527 *Geophys. Res.*, 75, 4997–5009.

528 Castro, R. R., Pacor, F., Puglia, R., Ameri, G., Letort, J., Massa, M., & Luzi, L. (2013). The 2012  
529 May 20 and 29, Emilia earthquakes (Northern Italy) and the main aftershocks: S-wave  
530 attenuation, acceleration source functions and site effects. *Geophys. J. Int.*, 195(1), 597–611.  
531 <https://doi.org/10.1093/gji/ggt245>

532 Causse, M., Cultrera, G., Moreau, L., Herrero, A., Schiappapietra, E., & Courboux, F. (2017).  
533 Bayesian rupture imaging in a complex medium: The 29 May 2012 Emilia, Northern Italy,  
534 earthquake. *Geophys. Res. Lett.*, 44, 7783–7792, doi:10.1002/2017GL074698.

535 Cesca, S., Braun, T., Maccaferri, F., Passarelli, L., Rivalta, E., & Dahm, T. (2013). Source  
536 modelling of the M5–6 Emilia–Romagna, Italy, earthquakes (2012 May 20–29). *Geophys. J.*  
537 *Int.*, 193, 1658–1672. <http://dx.doi.org/10.1093/gji/ggt069>.

538 Comité Européen de Normalisation (CEN), 2004. *Eurocode 8: Design of Structures for Earthquake*  
539 *Resistance—Part 1: General Rules, Seismic Actions and Rules for Buildings*, Comité  
540 Européen de Normalisation, Brussels.

541 Convertito, V., Catalli, F., & Emolo, A. (2013). Combining stress transfer and source directivity:  
542 the case of the 2012 Emilia seismic sequence. *Scientific Reports*, 3, 3114.  
543 <https://doi.org/10.1038/srep03114>

544 Convertito, V., Pino, N. A., & Di Luccio, F. (2016). Investigating source directivity of moderate  
545 earthquakes by multiple approach: the 2013 Matese (southern Italy)  $M_w = 5$  event. *Geophys.*  
546 *J. Int.*, 207, 1513-1528. <https://doi.org/10.1093/gji/ggw360>

547 Emolo, A., & A. Zollo (2005). Kinematic source parameters for the 1989 Loma Prieta earthquake  
548 from the nonlinear inversion of accelerograms. *Bull. Seismol. Soc. Am.*, 95(3), 981–994  
549 <https://doi.org/10.1785/0120030193>

550 Ganas, A., Roumelioti, Z., & Chousianitis, K., (2012). Static stress transfer from the May 20,  
551 2012, M 6.1 Emilia-Romagna (northern Italy) earthquake using a co-seismic slip  
552 distribution model, *Annals of Geophys.*, 55, 655-662, 2012; [http://doi.org/](http://doi.org/10.4401/ag-6176)  
553 [10.4401/ag-6176](http://doi.org/10.4401/ag-6176)

554 Gelman, A., Carlin B.J., Stern H.S., and D.B. Rubin (2004), *Bayesian Data Analysis*, Boca Raton,  
555 Fla.: Chapman & Hall/CRC. 2004. ISBN 978-1584883883.

556 Govoni, A., Marchetti, A., De Gori, P., Di Bona. M., Lucente, F. P., Improta L., Chiarabba, C.,  
557 Nardi, A., Margheriti, L., Piana Agostinetti, N., Di Giovambattista, R., Latorre, D., Anselmi,  
558 M., Ciaccio, M. G., Moretti, M., Castellano, C., & Piccinini, D. (2014). The 2012 Emilia  
559 seismic sequence (Northern Italy): imaging the thrust fault system by accurate aftershock  
560 location. *Tectonophysics*, 622, 44-55. <https://doi.org/10.1016/j.tecto.2014.02.013>

- 561 Graves, R. W., & Wald, D. J. (2001). Resolution analysis of finite fault source inversion using one-  
562 and three-dimensional Green's functions: 1. Strong motions. *J. Geophys. Res.*, *106*, 8745–  
563 8766. <https://doi.org/10.1029/2000JB900436>
- 564 Guatteri, M., Mai, P. M., Beroza, G., & Boatwright, J. (2003). Strong ground-motion prediction  
565 from stochastic–dynamic source models. *Bull. Seismol. Soc. Am.*, *93*(1), 301–313,  
566 <https://doi.org/10.1785/0120020006>
- 567 Guatteri, M., Mai, P. M., & Beroza, G. (2004). A pseudo-dynamic approximation to dynamic  
568 rupture models for strong ground motion prediction. *Bull. Seismol. Soc. Am.*, *94*(6), 2051–  
569 2063, <https://doi.org/10.1785/0120040037>
- 570 Kanamori, H., Thio, H-K., Dreger, D., & Hauksson E. (1992). Initial investigation of the Landers,  
571 California, earthquake of 28 June 1992 using TERRAScope. *Geophys. Res. Lett.*, *19*, 2267-  
572 2270, <https://doi.org/10.1029/92GL02320>
- 573 Király-Proag, E., Satriano, C., Bernard, P., & Wiemer S. (2019). Rupture process of the Mw 3.3  
574 earthquake in the St. Gallen 2013 geothermal reservoir, Switzerland. *Geophys. Res. Lett.*,  
575 *46*(14), 7990-7999. <https://doi.org/10.1029/2019GL082911>
- 576 Ide, S., and G. C. Beroza (2001), Does apparent stress vary with earthquake size?. *Geophys. Res.*  
577 *Lett.*, *28*, 3349–3352. <https://doi.org/10.1029/2001GL013106>
- 578 Lai, C.G., Bozzoni, F., Mangriotis, M.D., & Martinelli, M. (2012). Geotechnical aspects of May 20,  
579 2012 M5.9 Emilia earthquake, Italy. EUCENTRE, Report V.1.0.
- 580 Lancieri, M., Madariaga, R., & Bonilla F. (2012). Spectral scaling of the aftershocks of the  
581 Tocopilla 2007 earthquake in northern Chile. *Geophys. J. Int.*, *189*, 469–480.  
582 <https://doi.org/10.1111/j.1365-246X.2011.05327.x>

583 Liberatore, L., Sorrentino, L., Liberatore, D., & Decanini, L. D. (2013). Failure of industrial  
584 structures induced by the Emilia (Italy) 2012 earthquakes. *Eng. Fail. Anal.*, *34*, 629–647.  
585 <https://doi.org/10.1016/j.engfailanal.2013.02.009>

586 Liu, P., Custodio, S., & Archuleta, R. J. (2006). Kinematic inversion of the 2004 M 6.0 Parkfield  
587 earthquake including an approximation to site effects. *Bull. Seismol. Soc. Am.*, *96*(4B),  
588 S143-S158. <https://doi.org/10.1785/0120050826>

589 Madariaga, R. (1976), Dynamics of an expanding circular crack, *Bull. Seismol. Soc. Am.*, *66*, 639–  
590 666.

591 Mai, P. M., & Beroza, G. C. (2002). A spatial random-field model for complex earthquake slip. *J.*  
592 *Geophys. Res.*, *107*(B11), ESE 10-1-ESE 10-21. <https://doi.org/10.1029/2001JB000588>

593 Malagnini, L., Herrmann, R. B., Munafò, I., Buttinelli, M., Anselmi, M., Akinci, A., & Boschi, E.  
594 (2012). The 2012 Ferrara seismic sequence: Regional crustal structure, earthquake sources,  
595 and seismic hazard. *Geophys. Res. Lett.*, *39*, L19302. <https://doi.org/10.1029/2012GL053214>

596 Manfredi, G., Prota, A., Verderame, G. M., De Luca, F., & Ricci, P. (2013). 2012 Emilia  
597 earthquake, Italy: Reinforced Concrete building response. *Bull Earthq. Eng.*, *12*(5), 2275-  
598 2298. <https://doi.org/10.1007/s10518-013-9512-x>

599 Masi, A., Santarsiero, G., Gallipoli, M. R., Mucciarelli, M., Manfredi, V., Dusi, A. & Stabile, T. A.  
600 (2013). Performance of the health facilities during the 2012 Emilia (Italy) earthquake and  
601 analysis of the Mirandola hospital case study. *Bull. Earthq. Eng.*, *12*(5), 2419-2443.  
602 <https://doi.org/10.1007/s10518-013-9518-4>

603 Metropolis, N., Rosenbluth, A. W., Rosenbluth, M. N., Teller, A. H., & Teller, E. (1953). Equation  
604 of state calculations by fast computing machines. *J. Chem. Phys.*, *21*, 1087-1092.  
605 <https://doi.org/10.1063/1.1699114>



606 Mori, J. J., Abercrombie, R. E., & Kanamori, H. (2003). Stress drops and radiated energies of the  
607 Northridge aftershocks. *J. Geophys. Res.*, *108*(B11), ESE 13-1-ESE 13.12.  
608 <https://doi.org/10.1029/2000JB000474>

609 Mucciarelli, M. & Liberatore, D. (2014). Guest editorial: The Emilia 2012 earthquakes, Italy. *Bull.*  
610 *Earthq. Eng.*, *12*, 2111-2116. <https://doi.org/10.1007/s10518-014-9629-6>

611 Pezzo, G., Merryman, J.P., Tolomei, C., Salvi, S., Atzori, S., Antonioli, A., Trasatti, E., Novali, F.,  
612 Serpelloni, E., Candela, L., & Giuliani, R., 2013. Coseismic deformation and source  
613 modeling of the May 2012 Emilia (Northern Italy) earthquakes. *Seismol. Res. Lett.*, *84*  
614 (4),645–655. <http://dx.doi.org/10.1785/022012017>

615 Piatanesi, A., Cirella, A., Spudich, P., & Cocco, M. (2007). A global search inversion for  
616 earthquake kinematic rupture history: Application to the 2000 western Tottori, Japan  
617 earthquake. *J. Geophys. Res.*, *112*, B07314. <https://doi.org/10.1029/2006JB004821>

618 Piccinini, D., Pino, N.A., & Saccorotti, G. (2012). Source complexity of the May 20th, 2012,  
619 Mw=5.9 Ferrara (Italy) event. *Annals of Geophys.*, *55*, 569-573, <http://doi.org/10.4401/ag->  
620 6111

621 Pino, N. A., Mazza, S., & Boschi, E. (1999). Rupture directivity of the major shocks in the 1997  
622 Umbria-Marche (Central Italy) sequence from regional broadband waveforms. *Geophys.*  
623 *Res. Lett.*, *26*, 2101-2104. <https://doi.org/10.1029/1999GL900464>

624 Pino, N.A., Palombo, B., Ventura, G., Perniola, B. & Ferrari, G. (2008). Waveform modeling of  
625 historical seismograms of the 1930 Irpinia earthquake provides insight on 'blind' faulting in  
626 Southern Apennines (Italy). *J. Geophys. Res.*, *113*, B05303.  
627 <https://doi.org/10.1029/2007JB005211>.

628 Prieto, G. A., Thomson, D. J., Vernon, F. L., Shearer, P. M., & Parker, R. L., 2007. Confidence  
629 intervals for earthquake source parameters, *Geophys. J. Int.*, 168(3), 1227-1234.  
630 <https://doi.org/10.1111/j.1365-246X.2006.03257.x>

631 Rivera, L. & Kanamori, H., 2005. Representations of the radiated energy in earthquakes, *Geophys.*  
632 *J. Int.*, 162, 148–155, doi:10.1111/j.1365-246X.2005.02648.x

633 Scognamiglio, L., Tinti, E., & Quintiliani, M. (2006). Time Domain Moment Tensor [Data set].  
634 <https://doi.org/10.13127/TDMT>

635 Serpelloni, E., et al. (2012), GPS observations of coseismic deformation following the May 20 and  
636 29, 2012, Emilia seismic events (northern Italy): data, analysis and preliminary models, *Ann.*  
637 *Geophys.*, 55, 4, doi:10.4401/ag-6168

638 Snoke, J. A. (1987), Stable determination of (Brune) stress drops, *Bull. Seismol. Soc. Am.*, 77, 530–  
639 538.

640 Stucchi, M., Meletti, C., Montaldo, V., Crowley, H., Calvi, G. M., Boschi, E. (2011). Seismic  
641 hazard assessment (2003–2009) for the Italian building code. *Bull. Seism. Soc. Am.*, 101,  
642 1885–1911. <https://doi.org/10.1785/0120100130>

643 Somerville, P., et al. (1999). Characterizing crustal earthquake slip models for the prediction of  
644 strong ground motion. *Seismol. Res. Lett.*, 70(1), 59–80.  
645 <https://doi.org/10.1785/gssrl.70.1.59>

646 Tertulliani, A., Arcoraci, L., Berardi, M., Bernardini, F., Brizuela. B., Castellano, C., Del Mese, S.,  
647 Ercolani, E., Graziani, L., Maramai, A., Rossi, A., Sbarra, M., & Vecchi, M. (2012). The  
648 Emilia 2012 sequence: a macroseismic survey. *Annals of Geophys.*, 55, 4, doi: 10.4401/ag-  
649 6140

- 650 Tondi, R., Vuan, A., Borghi, A., & Argnani, A. (2019). Integrated crustal model beneath the Po  
651 Plain (Northern Italy) from surface wave tomography and Bouguer gravity data.  
652 *Tectonophysics*, 750, 262–279, doi:10.1016/j.tecto.2018.10.018
- 653 Ventura, G., and R. Di Giovambattista (2013). Fluid pressure, stress field and propagation style of  
654 coalescing thrusts from the analysis of the 20 May 2012  $M_L$  5.9 Emilia earthquake (northern  
655 Apennines, Italy). *Terra Nova*, 25, 72–78, doi:10.1111/ter.12007
- 656 Wells, D.L., & Coppersmith, K. J. (1994). New empirical relationships among magnitude, rupture  
657 length, rupture width, rupture area, and surface displacement. *Bull. Seism. Soc. Am.*, 84,  
658 974-1002
- 659 Wessel, P., & Smith, W. H. F. (1991). Free software helps map and display data. *Eos Trans. AGU*  
660 72, 441–446. <https://doi.org/10.1029/90EO00319>
- 661 Zollo, A., A. Orefice, and Convertito V. (2014), Source parameter scaling and radiation efficiency  
662 of microearthquakes along the Irpinia fault zone in southern Apennines, Italy. *J. Geophys.*  
663 *Res.*, 119, 3256–3275. <https://doi:10.1002/2013JB010116>.
- 664

665

666 **Table 1.** List of the stations used for the spectral fitting. The table contains the station code, stations  
667 coordinates, EC8 site classification (Comité Européen de Normalisation 2004), based on Vs30 – as  
668 reported by Castro et al. (2004) – and the managing institution. INGV refers to Istituto Nazionale di  
669 Geofisica e Vulcanologia, while DPC refers to Dipartimento della Protezione Civile Nazionale.

670

<b>Station code</b>	<b>Lat(°)</b>	<b>Lon(°)</b>	<b>Elev.(m)</b>	<b>EC8 code</b>	<b>Network</b>
BRIS	44.225	11.767	260	A*	INGV
CPC	44.921	11.876	2	C*	DPC
FAEN	44.290	11.877	41	C	INGV
IMOL	44.360	11.743	27	C	INGV
MODE	44.630	10.949	41	C*	INGV
MDN	44.646	10.889	37	C	DPC
OPPE	45.308	11.172	20	C*	INGV
TREG	45.523	11.161	342	C*	DPC

671

672

673

674

675

676

677

678

679

680

681

682 **Figure caption**

683 **Figure 1:** Geographic map showing the location of the May 20,  $M_L$  5.9 ( $M_w$  5.8), the May 29,  $M_L$   
684 5.8 ( $M_w$  5.8), Po Plain (Northern Italy) earthquakes. The black circles, whose dimension in  
685 proportional to the magnitude, indicate the aftershocks occurred in the period 20-05-2012 to 02-06-  
686 2012 and relocated by Govoni et al. (2014). The stations used in the present study belong to distinct  
687 networks and are indicated in the inset as triangles (red: Istituto Nazionale di Geofisica e  
688 Vulcanologia; blue: Istituto Nazionale di Oceanografia e Geofisica Sperimentale; green: Università  
689 di Genova). The location of the May 19,  $M_L$  4.1 ( $M_w$  4.0), foreshock – used as empirical Greens’  
690 function in the present study – is also displayed with a red circle. The source mechanisms for the  
691 main event and for the empirical Greens’ function are shown and correspond to the best double-  
692 couple of the TDMT solutions (<http://cnt.rm.ingv.it/tdmt.html>, Scognamiglio et al., 2006).

693

694 **Figure 2:** Examples of waveforms for the main shock (top trace) and the EGF (bottom trace). The  
695 STF obtained from the deconvolution is shown in the inset. Each panel shows station codes, as  
696 indicated in Figure 1, along with the azimuth of the receiver relative to the source epicentre.

697

698 **Figure 3:** Black: STFs obtained by the deconvolution of the selected EGF. The vertical dashed line  
699 marks the time  $t=0$ . The stations code, the epicentral distance in km, and the source-to-receiver  
700 azimuth are also reported. Grey: apparent moment rates predicted at fixed azimuths (indicated on the  
701 right). Each column displays the synthetic apparent STFs for the moment rate functions reported on  
702 the top of it, in the inset. All the ruptures are assumed to last 7 s and propagate at 2.2 km/s toward the  
703 azimuth indicated on each assumed source function.

704

705 **Figure 4:** (a) Final slip map for the May 20,  $M_w$  5.8, Po Plain (Northern Italy) earthquake  
706 corresponding to the synthetic STFs shown in Figure 5. The grey crosses identify the location of the  
707 control points while the white star represents the nucleation point position. (b) Static stress drop map  
708 obtained from the slip map distribution. White crosses correspond to the aftershocks relocated by

709 Govoni et al. (2014). (c) Fracture energy computed by using the approach of Guatteri et al. (2004).

710

711 **Figure 5:** Observed source time functions (black lines) and synthetic (red lines) source time functions  
712 corresponding to the best solution obtained from the Bayesian inverse approach. The grey bands  
713 correspond to the STFs obtained from the model used to compute the mean slip map shown in Figure  
714 7. In each panel the station code, the source-to-station azimuth, and correlation coefficient (bold) are  
715 reported.

716

717 **Figure 6:** Spectra of the observed (black lines) and synthetic (red lines) source time functions  
718 corresponding to the best solution obtained from the Bayesian inverse approach. The grey curves  
719 correspond to the minimum and maximum at each frequency of the STFs obtained from the model  
720 used to compute the mean slip map shown in Figure 7. In each panel the station code, the source-to-  
721 station azimuth, are reported.

722

723 **Figure 7:** Average model (panel a) and standard deviation model (panel b) from ensemble inference.

724

725 **Figure 8:** Map showing the location of the stations available for the spectral fitting (grey triangles)  
726 and those used to infer the best parameters (black triangles). The star identifies the epicenter of the  
727 May 20,  $M_L$  5.9 ( $M_w$  5.8). The side panels show the observed acceleration spectra (black line, green  
728 line and blue line) at the stations indicated in the panel, the best fit spectra (red dashed line), and the  
729 pre-P spectrum of the noise (grey line, green line and blue line).

730

731

732

Figure 1.

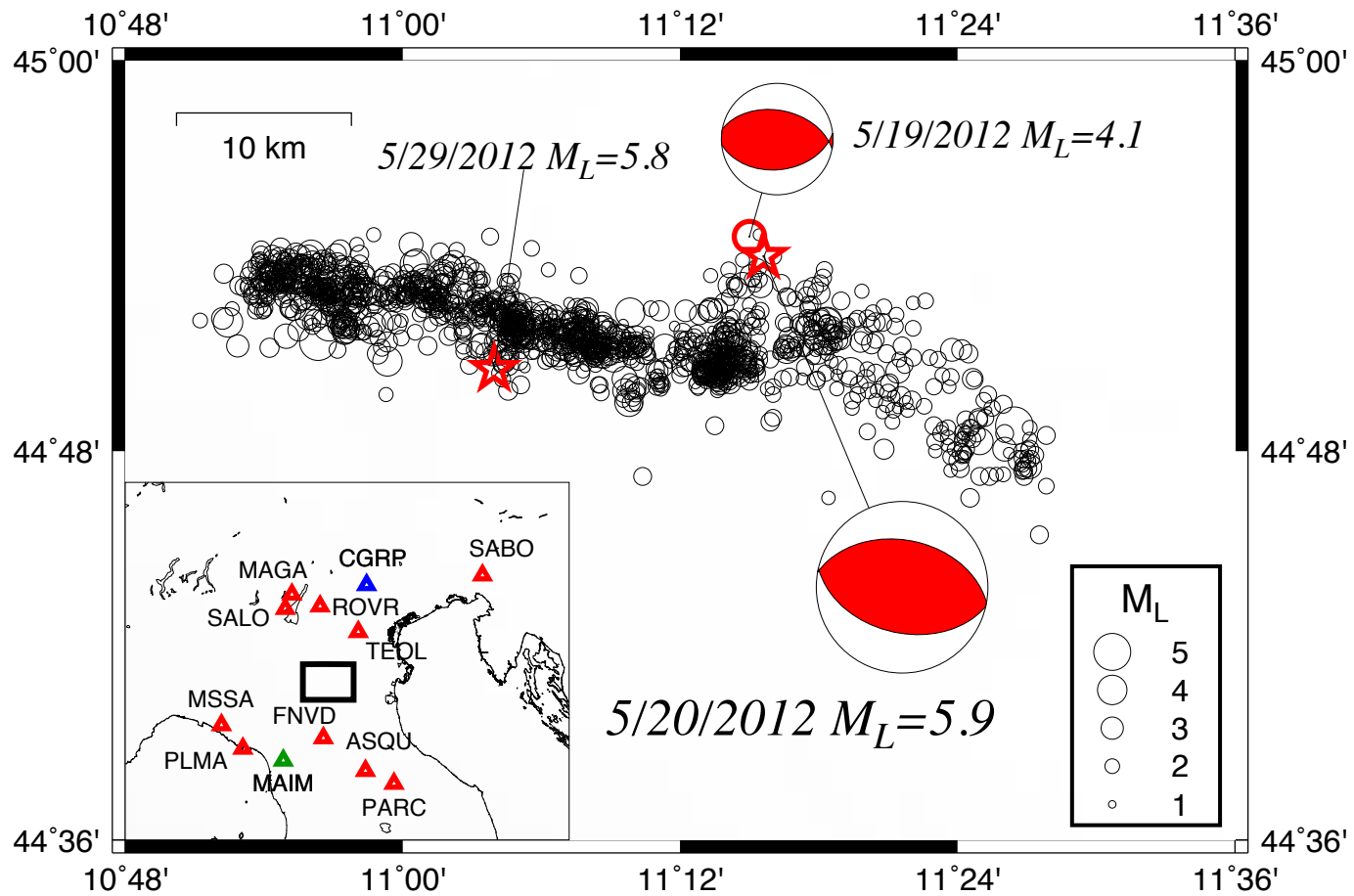




Figure2.

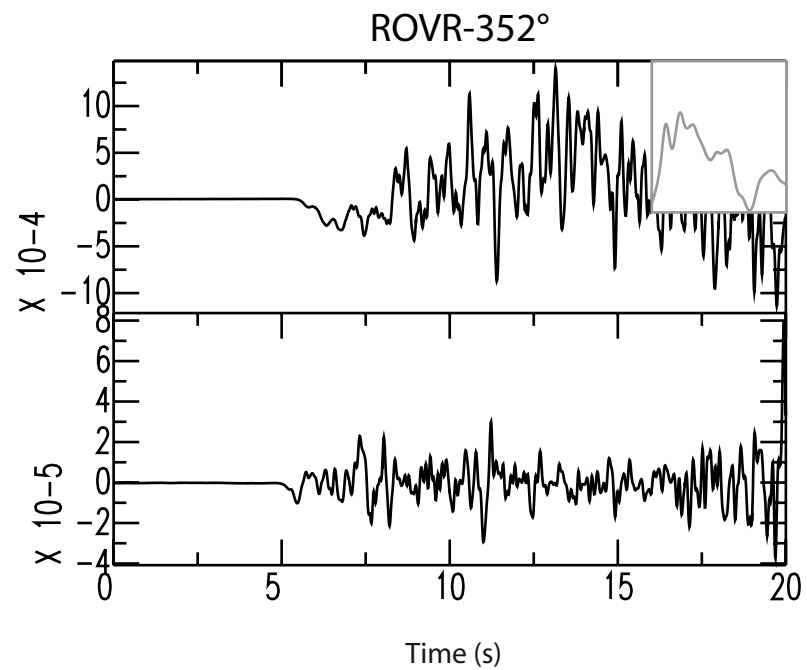
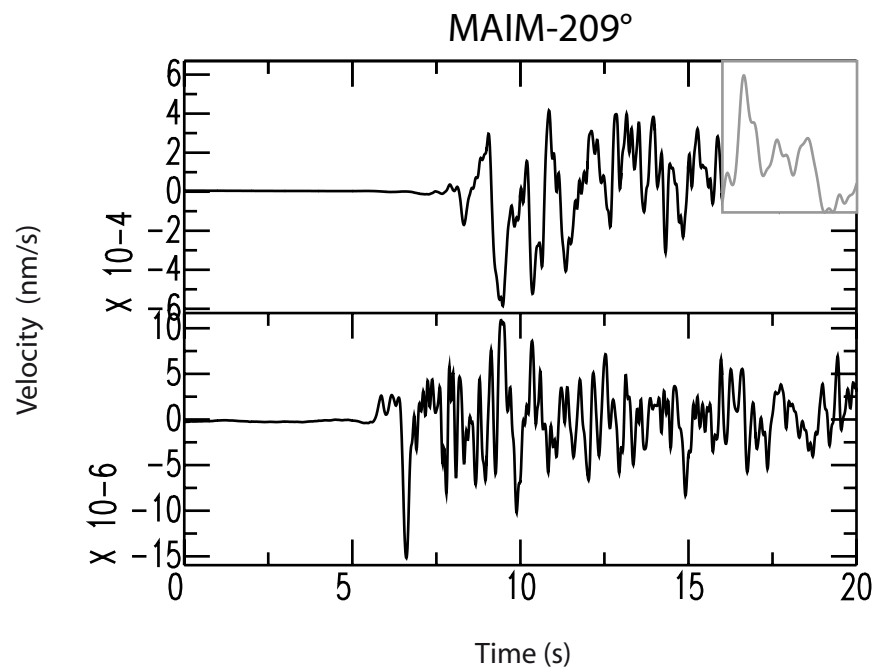
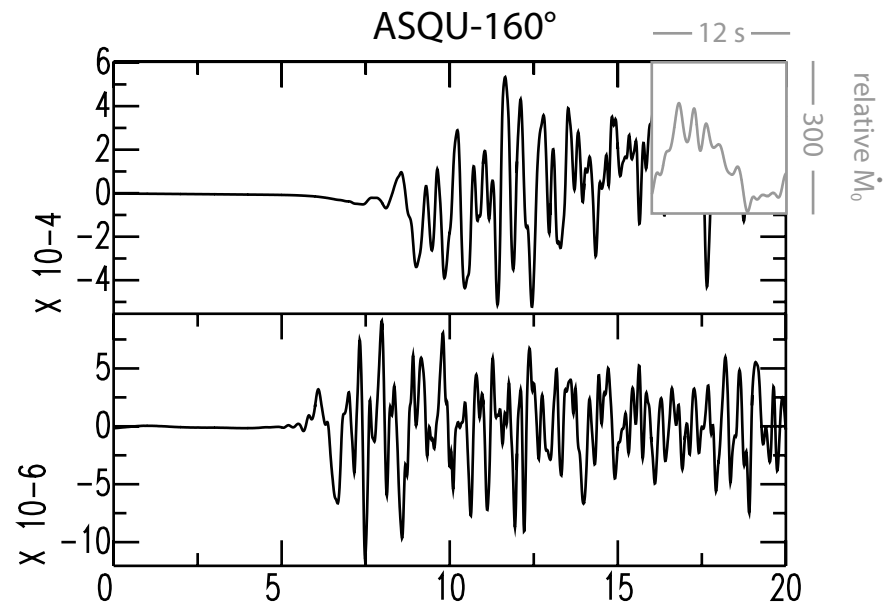
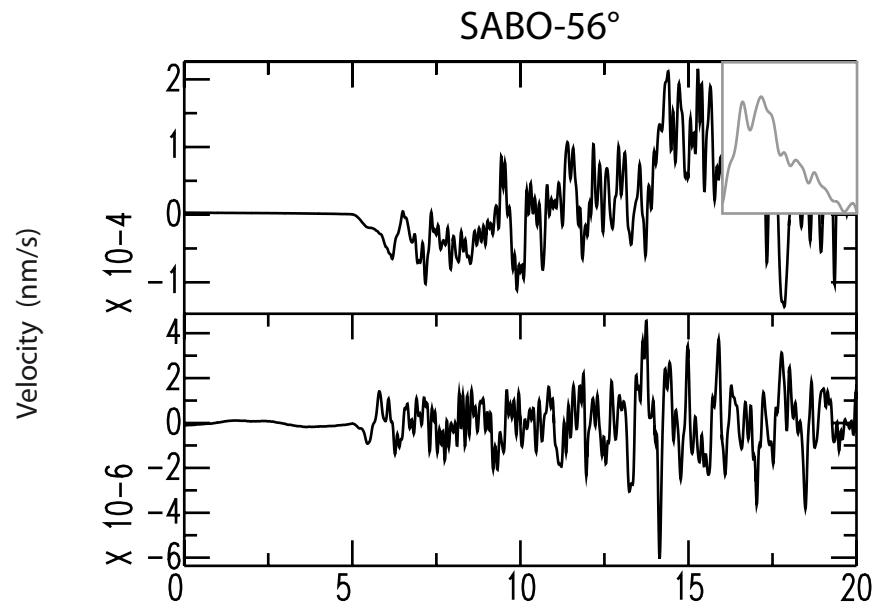
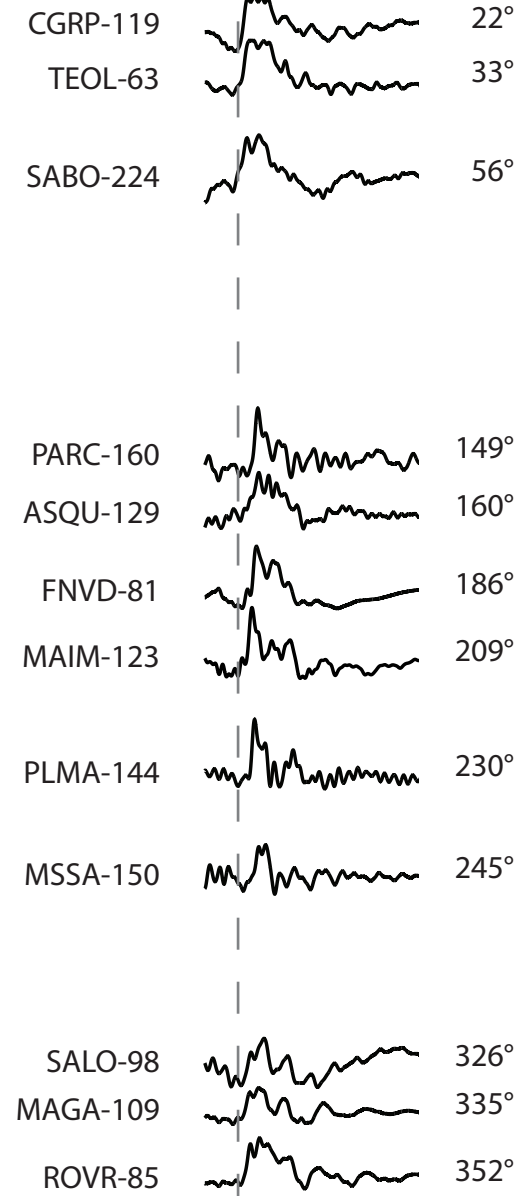


Figure3.

5 s

Data



Sources

( $\tau=7$  s  $v_r=2.2$  km/s)

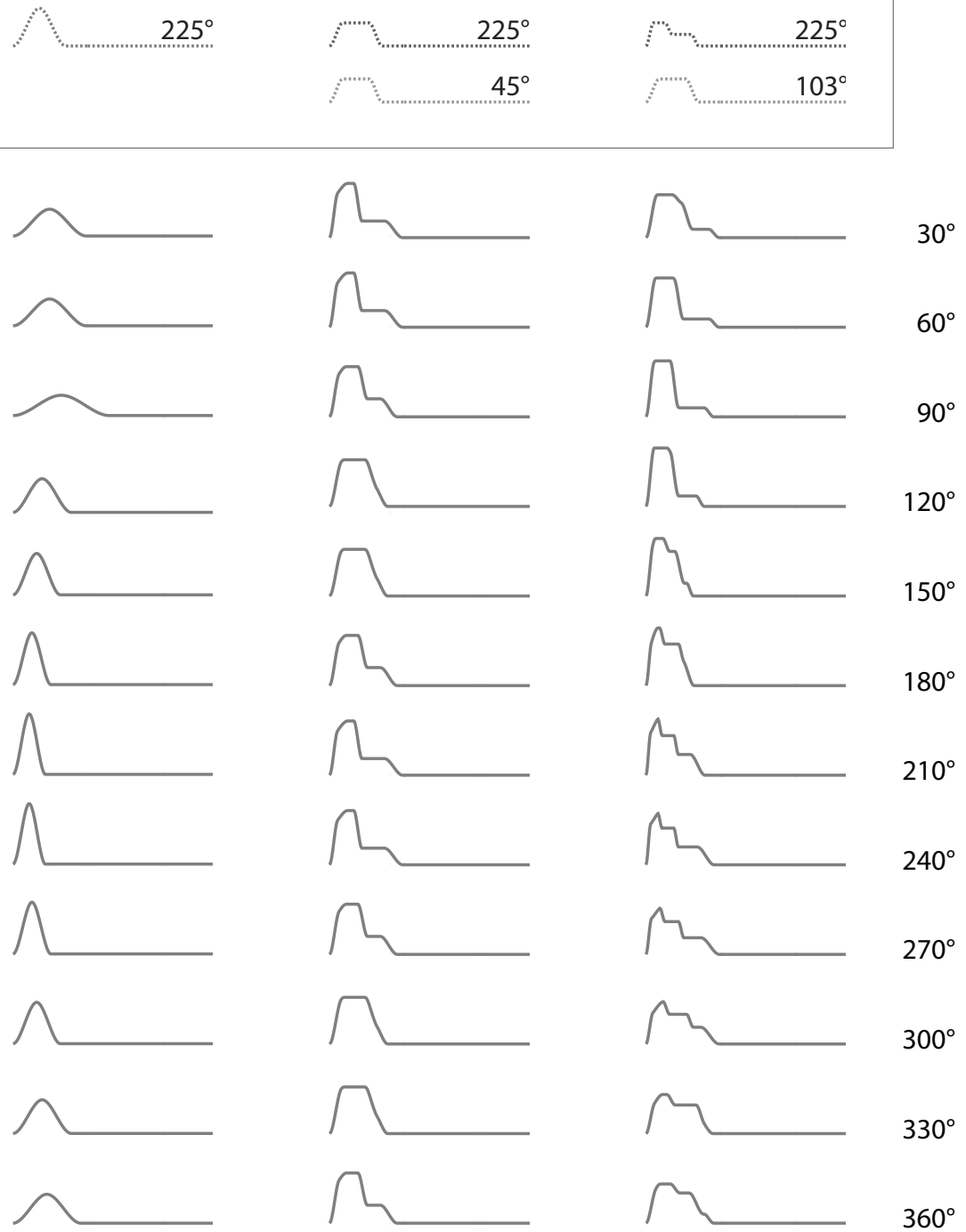


Figure4.

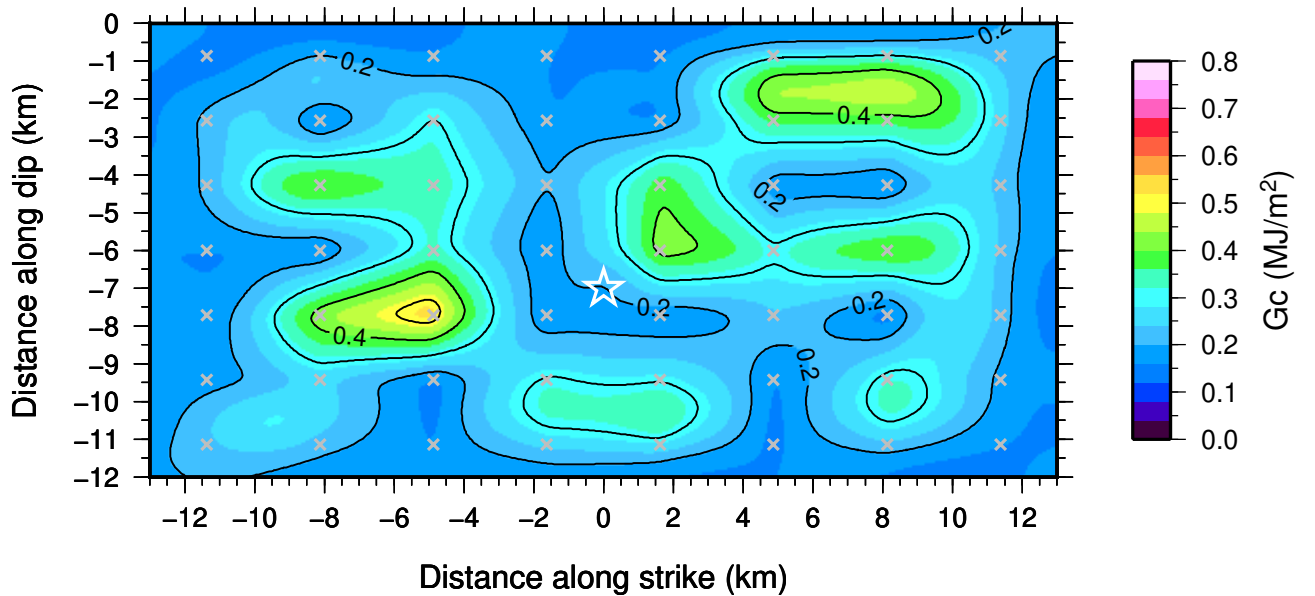
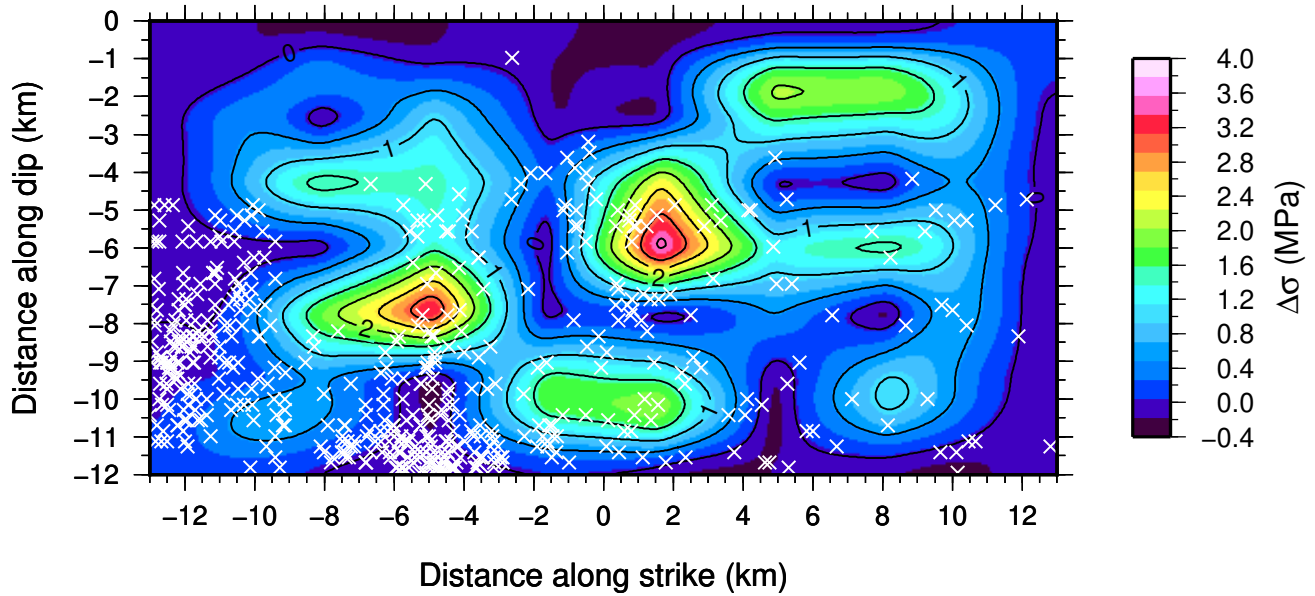
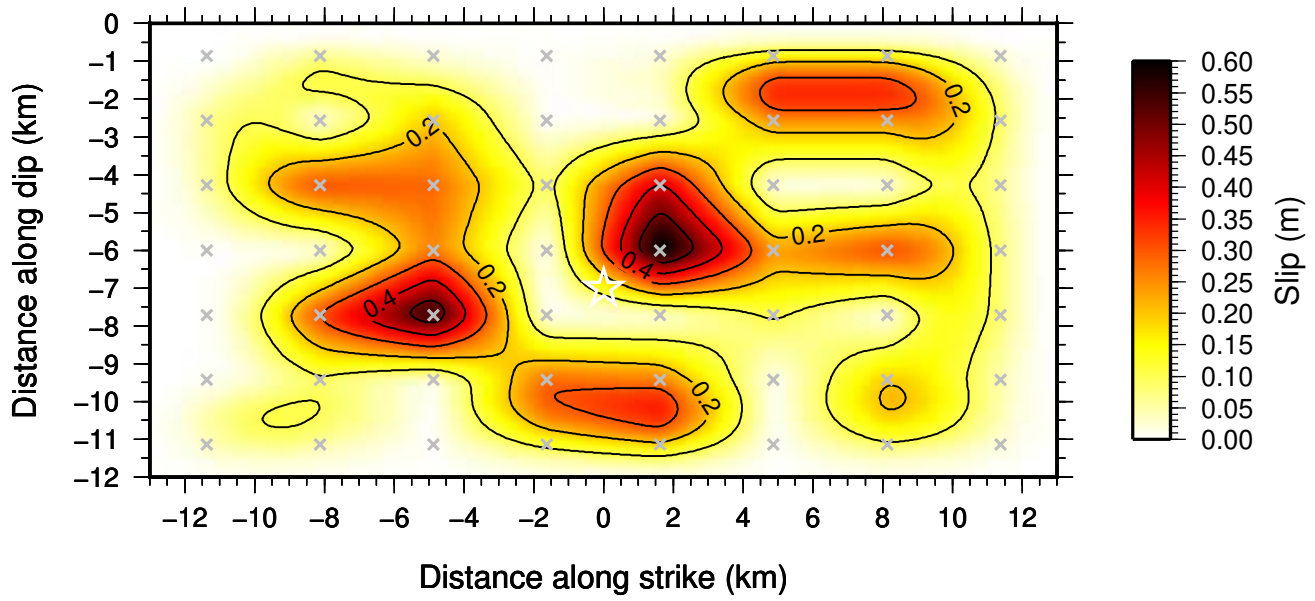


Figure5.

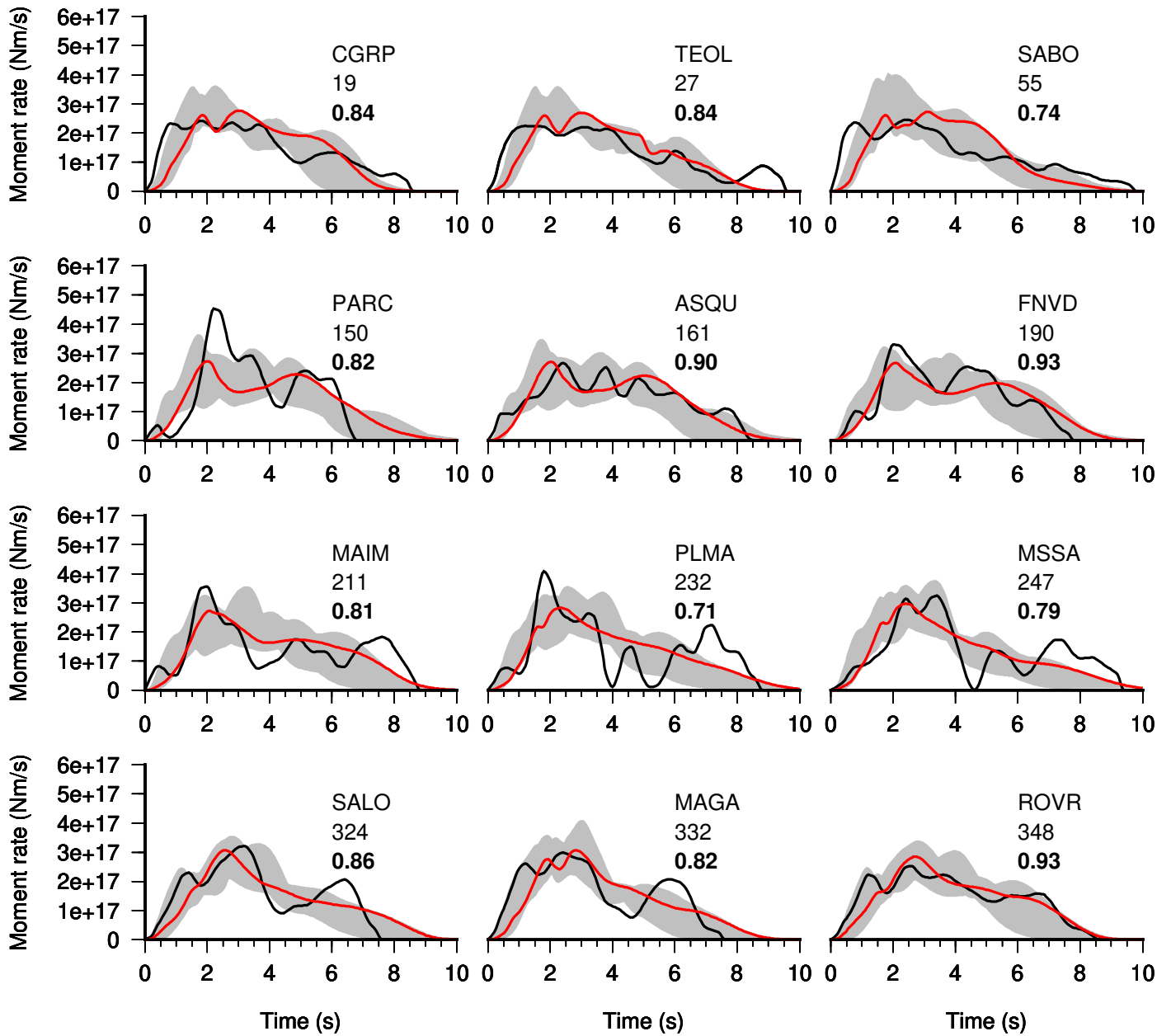




Figure6.

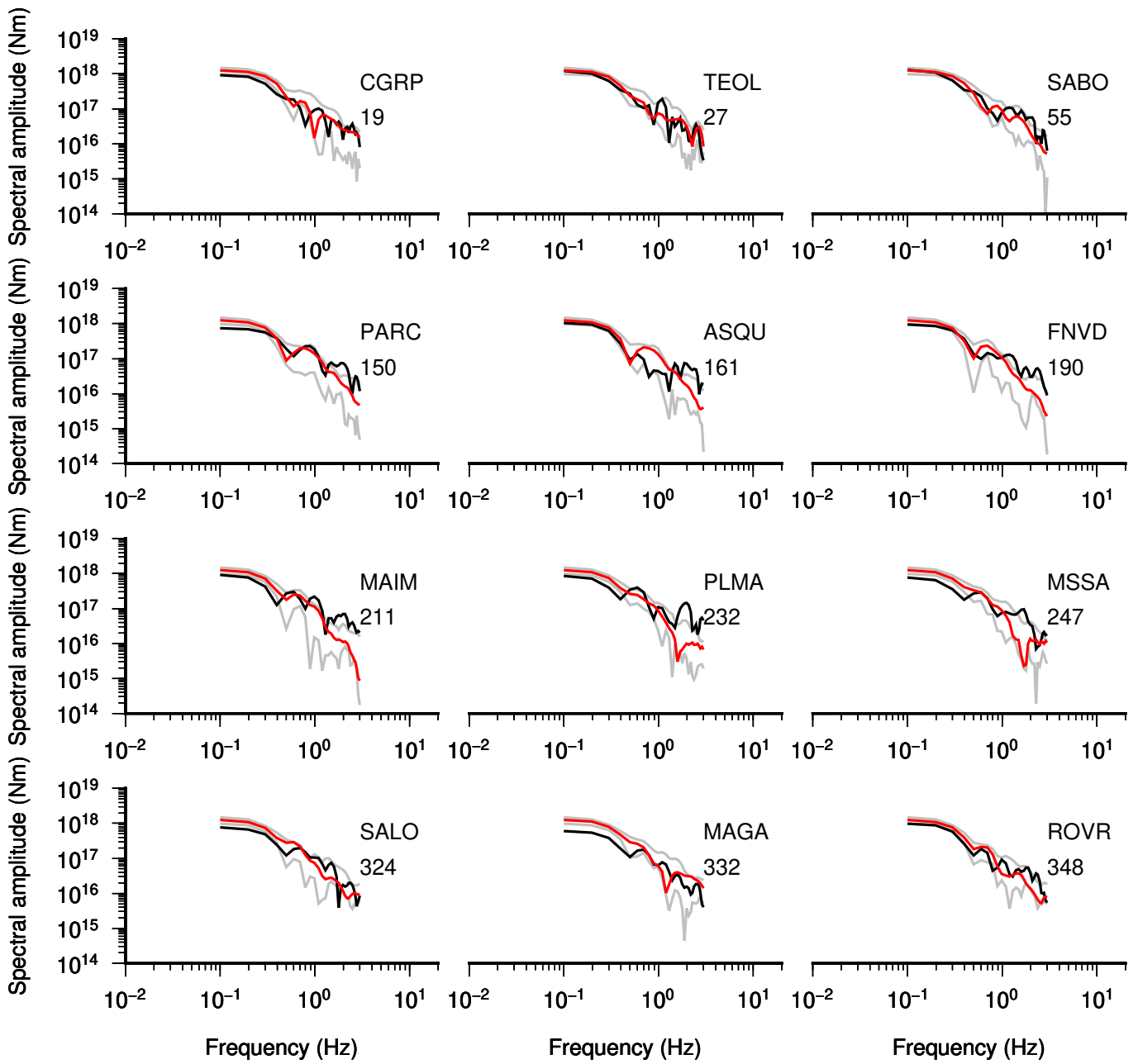


Figure 7.

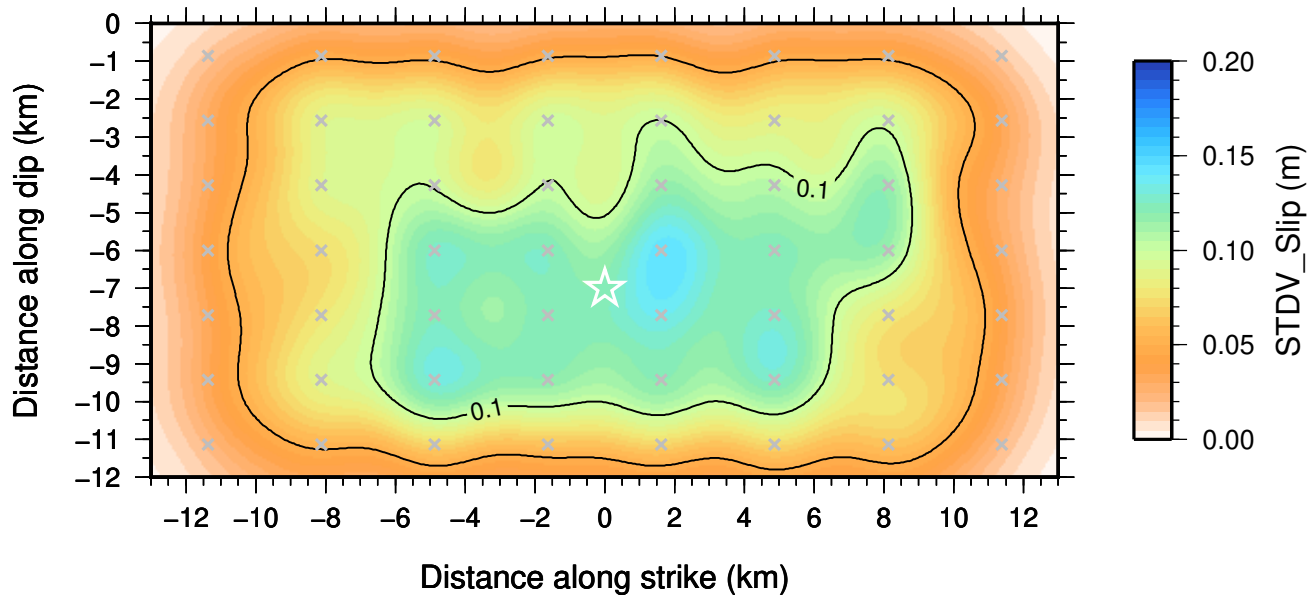
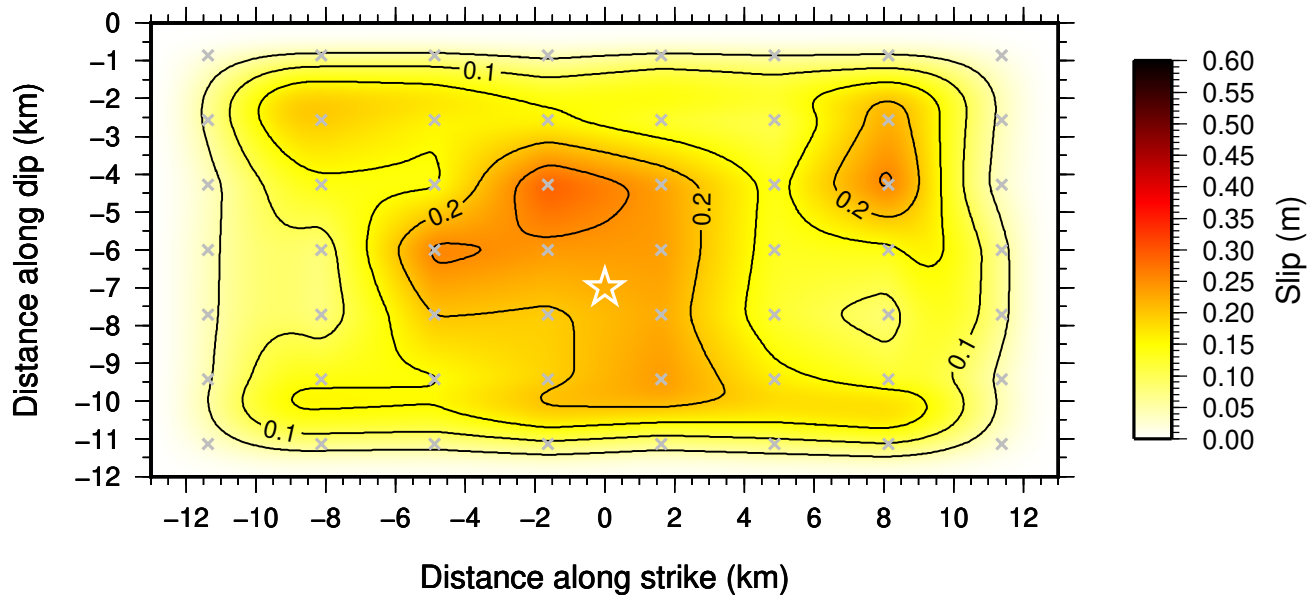


Figure 8.

